2011-01-01

Magnetic And Structural Properties Of Zinc-Doped Nickel Ferrite

Kanokporn Chattrakun
University of Texas at El Paso, k.chattrakun@gmail.com

MAGNETIC AND STRUCTURAL PROPERTIES OF

ZINC-DOPED NICKEL FERRITE

KANOKPORN CHATTRAKUN

Department of Physics

APPROVED:

_____

Cristian E. Botez, Ph.D., Chair

_____

Felicia Manciu, Ph.D.

_____

Geoffrey B. Saupe, Ph.D.

_____

Patricia D. Witherspoon, Ph.D.
Dean of the Graduate School

MAGNETIC AND STRUCTURAL PROPERTIES OF ZINC-DOPED NICKEL FERRITE

By

KANOKPORN CHATTRAKUN

THESIS

Presented to the Faculty of the Graduate School of

The University of Texas at El Paso

in Partial Fulfillment

of the Requirements

for the Degree of

MASTER OF SCIENCE

Department of Physics

THE UNIVERSITY OF TEXAS AT EL PASO

May 2011

ACKNOWLEDGEMENTS

It is my distinguished pleasure to thank my advisor, Dr. Cristian Botez, for his endless guidance, support, and patience. His assistance has been a vital component throughout the completion of this work and the course of the program. It has been an honor to work with him during the past two years and I am also proud to have been part of his research group.

I would like to also thank Dr. Felicia Manciu, and Dr. Geoffrey Saupe for serving on my committee and for their invaluable suggestions. My thanks also go to Dr. Vivian Incera for her help and encouragement since the beginning of my time here at the Physics Department of the University of Texas at El Paso, and for giving me this great chance to be a graduate student.

I would also like to extend a special thanks to my family who have always been there for me and continuously supported me even though I am so far from home. Finally, I would like to thank Alfonso Rodriguez for his supporting mind and his hand in helping me throughout this work.

ABSTRACT

We have used dc-magnetization, ac-magnetic susceptibility and x-ray diffraction (XRD) to investigate the microscopic origin of the magnetic property modifications induced by zinc doping in bulk and nano-sized nickel ferrite. Magnetic measurements indicate that the nanoparticle energy barrier to magnetization reversal, E_B, and the bulk saturation magnetization, M_s, follow similar dependences on the zinc doping fraction, x. Both these magnetic quantities initially increase with increasing x, reach a maximum at x~0.5, and eventually decrease upon further doping. Synchrotron and laboratory powder XRD data show no evidence of significant structural modifications for x~0.5: we find the lattice parameter of $Zn_xNi_{1-x}Fe_2O_4$ to exhibit a linear increase with x, and the inverse spinel crystal structure of $NiFe_2O_4$ (x=0) to persist throughout the entire zinc doping range $\mathbf{0 \leq x \leq 1}$. Instead, A- and B- site occupancy refinements via Rietveld analysis reveal an indirect mechanism by which Ni^{2+} ions, which reside in B (octahedral) sites, are replaced by Zn^{2+}. In this scenario, zinc is incorporated into A (tetrahedral) sites where it displaces Fe^{3+} ions, which migrate to the B sub-lattice and replace Ni^{2+}. This doping mechanism is consistent with the observed magnetic property enhancement at x~0.5.

TABLE OF CONTENTS

Page

LIST OF TABLES

LIST OF FIGURES

CHAPTER 1

INTRODUCTION

Complex spinel ferrites, $M1_xM2_{1-x}Fe_2O_4$ (M1, M2 = Co, Mg, Zn, Ni, Mn) are materials of great interest due to the possibility of tuning their macroscopic properties via chemical manipulation [1]. This is particularly important for magnetic materials, as several quantities related to the application of these systems in key technological fields, such as magnetic data recording and bio-medicine could be enhanced by divalent cation doping. Many studies have proposed effective synthesis procedures of complex spinel ferrites and successfully demonstrated the cation-doping induced modification of the system's magnetic properties [2]. Unfortunately, however, the microscopic structures and mechanisms underlying this behavior have not been investigated thoroughly and, consequently, are not fully understood. From this perspective, $Zn_xNi_{1-x}Fe_2O_4$ ($0 \leq x \leq 1$) is a particularly interesting system. Indeed, previous studies have shown that adding Zn^{2+} ions to spinel ferrites has an unexpectedly strong effect on their magnetic properties despite the fact that Zn^{2+} ions are non-magnetic [3]. In addition, the magnetic property enhancement upon Zn doping is not restricted to bulk nickel ferrite, but also occurs in $Zn_xNi_{1-x}Fe_2O_4$ nanoparticles [4]. These observations render $Zn_xNi_{1-x}Fe_2O_4$ as a particularly suitable system for investigating not only the microscopic details that govern the modification of magnetic properties of complex spinel ferrites upon cation doping, but also the extent to which this magnetic behavior is affected by size related effects such as the surface to volume ratio increase related to the reduction of the material's crystalline grains in $Zn_xNi_{1-x}Fe_2O_4$ nanoparticles.

Here we present a detailed investigation of bulk and nanosized $Zn_xNi_{1-x}Fe_2O_4$ aimed at gaining more insight into the microscopic structures and mechanisms responsible for the magnetic property modification of this complex ferrite upon zinc doping. Uncovering such microscopic details is clearly an important step towards reaching the ultimate goal of this research, namely the ability to rationally design bulk and nanoferrites with enhanced magnetic properties. Our dc-magnetization and ac-magnetic-susceptibility measurements reveal that *both* the energy barrier to magnetization reversal of a 10-nm average sized nanoparticle ensemble, E_B, *and* the saturation magnetization of bulk $Zn_xNi_{1-x}Fe_2O_4$, M_s, display a very similar and specific dependence on the zinc doping fraction, x. These magnetic quantities initially increase with increasing x, then reach a maximum at x~0.5, and eventually decrease upon further doping. To uncover the microscopic origin of this behavior we collected powder XRD data on the $Zn_xNi_{1-x}Fe_2O_4$ series and analyzed it using Le Bail [5] and Rietveld refinement methods [6]. We found no evidence of significant structural modifications for x~0.5. Instead, our structural analysis indicates that the magnetic behavior observed upon zinc doping stems from an indirect mechanism of Ni replacement that leads to two competing magnetocrystalline effects that crossover at x~0.5. This scenario appears to occur in both bulk and nano-sized $Zn_xNi_{1-x}Fe_2O_4$ which indicates that the doping induced enhancement of the barrier to magnetization reversal in the nanoparticle ensemble is not related to the large surface-to-volume ratio of this system.

CHAPTER 2

THEORETICAL BACKGROUND

2.1 Basic Magnetism

2.1.1 Magnetization

Magnetization is defined as the amount of magnetic moment per unit volume of the material.

$$\vec{M} = \frac{d\vec{\mu}}{dV} \tag{2.1}$$

$\vec{\mu}$ is the quantity of magnetic moment vector and V is the volume of material.

The net magnetization results from the response of the material in an external magnetic field [7]. Magnetization also depends on the purity of the material as well as other factors. For ferromagnetic materials, there will be saturation in the magnetization. The effect occurs due to the fact that the core can make no further contribution to the flux growth and any increase thereafter is limited. This is called saturation magnetization.

2.1.2 Magnetic Moment

The magnetic moment is defined in MKS units by the equation

$$\vec{\mu} = I\vec{a} \tag{2.2}$$

The MKS system is defined so that the unit of length is meter, the unit of mass is kilogram and the unit of time is second. Here $\vec{\mu}$ is the magnetic moment vector, and $\vec{a}$ is the vector area of the current loop; if the loop is flat, then $\vec{a}$ is the ordinary area enclosed, with the direction assigned by the usual right hand rule.

The magnetic moment in electrostatics is equivalent to the magnetic dipole moment since it is the dominant term and the magnetic monopole is always zero. The system with a net magnetic dipole moment will produce a net magnetic field which can be measured.

2.1.3 Magnetic Field

Magnetic field in magnetostatics is produced by a steady current. The magnetic field is given by the Biot-Savart law

$$\vec{B}(\vec{r}) = \frac{\mu_0}{4\pi}\int \frac{\vec{I}\times\hat{r}}{r^2} dl' = \frac{\mu_0}{4\pi} I \int \frac{d\vec{l'}\times\hat{r}}{r^2} \tag{2.3}$$

The integration is along the current path, in the direction of the flow. Here $d\vec{l'}$ is an element of length along the wire and $\hat{r}$ is the unit vector of the direction from the source to the observation point. The constant μ_0 is called the permeability of free space and has a value of

$\mu_0 = 4\pi \times 10^{-7} \frac{N}{A^2}$. This gives rise to the unit of magnetic field which is given in Newton per ampere-meter or tesla (T)

$$1T = 1 \frac{N}{A \cdot m} \text{ and 1 T is 10000 Oe} \tag{2.4}$$

There is another way to calculate the magnetic field generated from current loops that have appropriate symmetry called Ampere's law. Ampere's law is given in integral form as

$$\oint \vec{B} \cdot d\vec{l} = \mu_0 I_{enclosed} \tag{2.5}$$

The direction of the field in this case can be found by using the right hand rule.

2.1.4 Magnetic Field Intensity

The magnetic field generated from the calculation using Biot-Savart or Ampere's law is denoted by $\vec{B}$. When the generated magnetic field passes through a magnetic material, which itself has magnetic field, the individual contribution is difficult to differentiate. The new defined term used to describe the field is called magnetic field intensity or magnetic field strength denoted by $\vec{H}$ and defined by

$$\vec{H} = \frac{1}{\mu_0} \vec{B} - \vec{M} \tag{2.6}$$

Here $\vec{B}$ is the external magnetic field, and $\vec{M}$ is the magnetization of the material.

2.1.5 Faraday's Law

Faraday's law stems from empirical data. The law states that "a changing magnetic field induces an electric field". This can be expressed in terms of an equation derived from

$$\varepsilon = \oint \vec{E} \cdot d\vec{l} = -\frac{d\Phi}{dt} \tag{2.6}$$

Here ε is the electromotive force or EMF, $\vec{E}$ is the electric field, $\overrightarrow{dl}$ is the element of length and $d\Phi$ is the flux of the field. Also $\vec{E}$ is related to the change of $\vec{B}$ by

$$\oint \vec{E} \cdot d\vec{l} = -\int \frac{\partial \vec{B}}{\partial t} \cdot d\vec{a} \tag{2.7}$$

By appling Stokes' theorem we can write Faraday's law in integral form as

$$\nabla \times \vec{E} = -\frac{\partial \vec{B}}{\partial t} \tag{2.8}$$

2.1.6 Types of Magnetic Materials

Diamagnetic materials consist of atoms or molecules that have no net angular momentum [8]. In other words, one can say that diamagnetic materails have negative magnetic susceptibility or the magnetic susceptibility is less than the magnetic susceptibility in vacuum. Thus, diamagnetism is a very small effect. All materials can exhibit diamagnetism.

Paramagnetic materials include atoms that have a net angular momentum from unpaired electrons. Paramagnetic materails have positive magnetic susceptibility that is greater than the magnetic susceptibility in vacuum. The magnetic moment from odd electrons aligns with the

applied external magnetic field [9]. The magnetization of paramagnetic materials is not retained once the external magnetic field is removed.

Ferromagnetic materials are actually paramagnetic, but have a different interaction between atoms, which changes in the behavior drastically. There is no linear relation between the magnetic field $\vec{B}$ and $\vec{H}$. The application of an external field tends to cause the magnetic domains to change and the magnetic moments in different domains to line up together. Removal of the field leaves some fraction of these moments still aligned, which results in the permanent magnetization of these materials.

Ferrimagnetic materials are similar to ferromagnetic materials, except that not all of the magnetic moments are parallel to each other as in ferromagnet. The magnetic moments not contributing to the net spontaneous magnetization are oriented in random directions.

2.1.7 Magnetic Nanoparticles and Superparamagnetism

Superparamagnetism is an interesting phenomenon that occurs in ferromagnetic nanoparticle ensemble and is based on the fact that the formation of magnetic domain walls becomes energetically unfavorable. In this case, all moments in a particular particle will be aligned in the same direction. Hence every particle is a single domain, acting as a single colossal magnetic moment (the super spin). As in paramagnets, there will be some temperature at which the superspin possesses enough thermal energy to rotate freely and align with an external field. Below this temperature, the particles will not be able to rotate freely, and are referred to as blocked. This type of magnetic behavior is called superparamagnetism [10]. Many ferromagnetic nanoparticles show such behavior.

2.1.8 Vogel-Fulcher Formalism

The Vogel-Fulcher law is used to describe the magnetic relaxation of a nanoparticle system, and other magnetic systems. Theoretically this law accounts for some slight inter-particle interactions. An interesting thing to note is that, while the VF equation has been confirmed experimentally to model many types of systems (supercooled organic liquids, spin glasses, polymers), there is still no widely accepted derivation of the law from first principles to a mesoscopic level. The simplest form of the Vogel-Fulcher equation is of the form

$$\tau = \tau_0 e^{\left(\frac{E_B}{k_B(T-T_0)}\right)} \tag{2.9}$$

where τ is the average time it takes for a ferromagnetic cluster to randomly flip directions as a result of thermal fluctuations, τ_0 is a characteristic time of the material, k_B is the Boltzmann constant, T is the temperature**,** T_0 is a material specific characteristic temperature that accounts for inter-particle interactions**,** and E_B is the magnetic anisotropy energy, (the energy barrier associated with the magnetization moving from its initial "easy axis" direction, through a "hard axis", ending at another easy axis). E_B is directly proportional to a material specific anisotropy constant and particle volume [11], [12].

2.1.9 DC-Magnetization and AC-Magnetic-Susceptibility

The AC/DC Magnetometry System (ACMS) on the Quantum Design Physical Property Measurement System (Quantum Design, Inc., San Diego, CA, USA) is used to perform the DC magnetization, and AC-magnetic-susceptibiliy measurements of the samples. DC-magnetization measurement is the measurement which is performed to obtain magnetizations of materials by applying a direct current to a coil in order to generate a magnetic field. The generated field, thus,

is a constant field. To measure the magnetization of the magnetized samples, the samples have to be moved, which is done by the attached motor on top of the dewar. Moving a magnetized sample through the detection coils induces a voltage in the detection coil set. The amplitude of this signal is proportional to the magnetic moment and speed of the sample during extraction.

AC-magnetic measurements are measurements where an AC field is applied to a sample and the resultant moment is determined. It is an important tool for materials characterization, especially for time-dependent induced moment measurements which cannot be obtained from the DC-measurements. In AC magnetic measurements, a small AC drive magnetic field is applied, causing a time-dependent moment in the sample. The field of the time-dependent moment induces a current in the pickup coils, allowing the measurement to be performed without sample motion.

2.2 X-ray Diffraction

2.2.1 Crystal Structure

A crystal is formed by adding atoms or groups of atoms in a geometrical structure. The crystal develops as identical building blocks are added continuously. The building blocks are atoms or groups of atoms. The crystal includes a three dimensional periodic array of identical building blocks, apart from any imperfections and impurities that may be included or built into the structure. An ideal crystal is constructed by the infinite repetition of identical groups of atoms. This group is called the basis. The set of mathematical points to which the basis is attached is called the lattice. The lattice in three dimensions is defined by three translation

vectors: $\vec{a}_1, \vec{a}_2, \vec{a}_3$. The position of the center of an atom j of the basis relative to the associated lattice point is defined as follows [13].

$$\vec{r_j} = x_j\vec{a}_1 + y_j\vec{a}_2 + z_j\vec{a}_3 \tag{2.10}$$

2.2.2 Miller Indices

Miller indices are indices used to specify the orientation of a plane and are determined by the following rules:

- Find the intercept on the axis in terms of the lattice constants a_1, a_2, a_3.
- Take the reciprocals of these numbers and then reduce them to three integers having the same ratio, usually the smallest three integers. The result, enclosed in parentheses (hkl), is called the Miller index of the plane.

In cubic crystals the direction of [hkl] is perpendicular to a plane (hkl) having the same indices, but this is not generally true in other crystal systems.

2.2.3 Crystal System

The point symmetry groups in three dimensions require the 14 different lattice types listed in Table 1. These are grouped for convenience into systems classified according to seven types of cells. The division into systems is expressed in the table in terms of the axial relations that describes the cells.

Table 1: The 14 lattice types in three dimensions [13]

System	Number of lattice	Restrictions on conventional cell axes and angles
Triclinic	1	$a_1 \neq a_2 \neq a_3$ $\alpha \neq \beta \neq \gamma$
Monoclinic	2	$a_1 \neq a_2 \neq a_3$ $\alpha = \gamma = 90^\circ \neq \beta$
Orthorhombic	4	$a_1 \neq a_2 \neq a_3$ $\alpha = \beta = \gamma = 90^\circ$
Tetragonal	2	$a_1 = a_2 \neq a_3$ $\alpha = \beta = \gamma = 90^\circ$
Cubic	3	$a_1 = a_2 = a_3$ $\alpha = \beta = \gamma = 90^\circ$
Trigonal	1	$a_1 = a_2 = a_3$ $\alpha = \beta = \gamma < 120^\circ, \neq 90^\circ$
Hexagonal	1	$a_1 = a_2 \neq a_3$ $\alpha = \beta = 90^\circ$ $\gamma = 120^\circ$

2.2.4 Bragg's Law

An atom can scatter x-rays, and if many atoms scatter waves together, the scattered waves can interfere. The interference fringes show the diffracted beams in specific directions. These directions are determined by the wavelength of the incident x-ray wave and the properties of the crystalline structure. Bragg's law is used to calculate this relationship [14]

$$2d \sin\theta = n\lambda \tag{2.11}$$

Here d is the spacing between planes of the crystal, θ is the angle between the incident wave and the scattered planes, n is an integral number, and λ is the wavelength of incident wave.

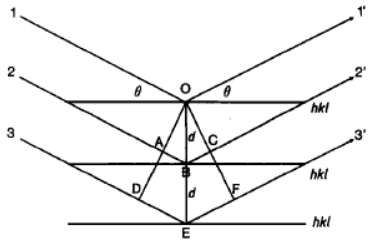

Figure 2.1 Diffraction of X-rays from planes in a crystal [15]

2.3.5 Inverse Spinel Crystal Structures-Nickel Ferrite

Spinels belong to a group of materials that have a chemical formula of $A^{2+}B_2^{3+}O_4^{2-}$. *A* represents a divalent metal ion while *B* represents a trivalent metal ion as shown by the oxidation number in the general form given beforehand [16]. The spinel crystal structure is the combination of cubic closed-packed, octahedral and tetrahedral substructures structures. The oxide anions reside in a cubic closed-packed lattice. The rest of the cations occupy the tetrahedral and octahedral sites in the lattice. The A^{2+}cations occupy 1/8 of the tetrahedral sites, while the B^{3+} cations occupy half of the octahedral sites because of the charge factor [17]. An inverse spinel whose structure is shown in figure 2.1 is the alternative arrangement of spinel in which half of the trivalent ions swap with the divalent ions. Zinc ferrite and nickel ferrite belong to this group. The difference between these two materials is that nickel ferrite has ferromagnetic properties, while zinc ferrite is antiferromagnetic.

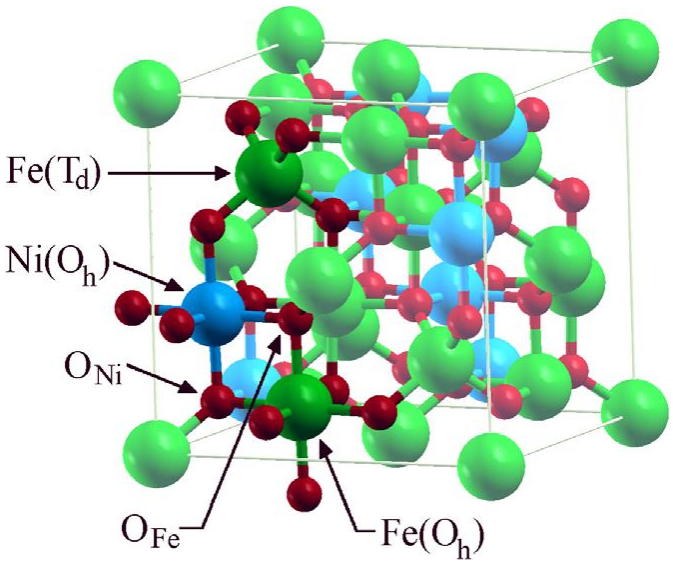

Figure 2.1: Inverse spinel structure of nickel ferrite [18]

Zinc-doped nickel ferrite is a mixed ferrite in which some of nickel is replaced by zinc. Interestingly, the macroscopic magnetic properties of these mixed ferrites are strongly influenced by the doping even when the dopant cation is non-magnetic.[2] It is necessary to analyze the microscopic details of doping into the structure of inverse spinel ferrites in order to explain the behavior of these materials' macroscopic properties.

2.3.7 Scherrer Formalism

Powder X-ray diffraction data is often used to calculate the average particle size of a nanoparticle sample, *D*, using Scherrer's formula, which relates the average nanoparticle size to the width of diffraction peaks at the half of its height, *FWHM*, the detector angle 2θ, the shape factor (a constant based of the geometry of the particles), and the wavelength of the incident X-rays, λ as follows.

$$D = \frac{0.89 \cdot \lambda}{\left(\frac{FWHM \cdot \pi}{180^\circ}\right) \cdot cos\left(\frac{2\theta}{2}\right)} \tag{2.12}$$

2.3.8 LeBail Analysis

LeBail analysis is used to perform full profile refinements of x-ray diffraction data without the atomic position being included [5]. This method is suited for finding the lattice parameter of the crystal structure. In order to carry the LeBail analysis, initial information about the unit cell and space group is needed. We used *FullProf* software to perform the Lebail analysis. *FullProf* is a program for profile refinement of x-ray powder diffraction data that has been developed based on a program initially written by Wiles and Young J. Applied Cryst.14, 149(1981), (DBW3.2S, Versions 8711 and 8804). The source is written in standard FORTRAN 77 language.

2.3.9 Rietveld Analysis

Rietveld refinement is a method of refining powder diffraction data developed by Hugo Rietved [6]. The refinement involves finding the complete sample's crystal structure, In order to perform the refinement, the initial information needed is atomic positions, fraction of atomic sites, lattice parameters, profile parameters, and background parameters. To carry out Rietveld refinements, we used the General Structure Analysis System (*GSAS*). *GSAS* is a set of programs for the processing and analysis of both single crystal and powder diffraction data obtained from x-rays diffraction. It is capable of handling all of these types of data simultaneously for a given structural problem. In addition, it can handle powder diffraction data from a mixture of phases and refine structural parameters for each phase. *GSAS* features a menu driven editor (*EXPEDT*) which is used to prepare all input for the main calculation programs in *GSAS*. The entire *GSAS* system is written in FORTRAN and uses some system callable features. An integral part of

GSAS is the facility for an interactive graphics display based on the PGPLOT graphical subroutine library in order to help plot analyzed data.

CHAPTER 3

EXPERIMENTAL PROCEDURE

3.1 Samples Synthesis

Bulk $Zn_xNi_{1-x}Fe_2O_4$ (x=0, 0.2, 0.4, 0.5, 0.6, 0.8, 1) ferrites were synthesized starting from high purity NiO, ZnO, and Fe_2O_3 powders. These precursors were weighed in appropriate stoichiometric ratios, then milled to an agate mortar for 30 minutes. Afterwards, the resulting powders were compacted into tablets by applying a pressure of 3 tons for 1 minute. The tablets were then sintered for 24 hours at 1100 ˚C. Heating and cooling rates of 10 °C/min. were used. Eventually, the samples were ground into fine powders. Nanoparticles of the title compound were prepared via a co-precipitation method, whereby stoichiometric amounts of $Ni(NO_3)_2{\cdot}6H_2O$, $Zn(NO_3)_2{\cdot}6H_2O$, and $FeCl_3{\cdot}6H_2O$ were dissolved in distilled water at room temperature with a NaOH precipitating agent solution. Phases were crystallized via one-hour digestion step at 90 °C and, eventually, the particles were thoroughly washed and dried at 60 °C.

3.2 Magnetic Measurement Setup - Quantum Design PPMS

The apparatus used in measuring the magnetization is the Physical Property Measurement System (PPMS) by Quantum Design. The particular PPMS model (Quantum Design, Inc., San Diego, CA, USA) we used can take measurements at temperatures ranging from from 1.9 K to 400 K, and magnetic fields as high as 7 T [19]. In our case, the experiments have to be done at

low temperatures and high fields. Liquid helium is used in the cooling system to cool both the sample, and the superconducting magnet generating the necessary magnetic field. The samples and the measuring instruments are enclosed in a dewar that is filled with liquid helium before use. Liquid nitrogen is used in the dewar's jacket to minimize the consumption of helium in the cooling system [20] as shown in the Figure 3.1.

The Quantum Design PPMS consists of a liquid nitrogen jacketed dewar, Model 6000 controller, a probe, top plate assembly, probe lifting assembly, electronics cabinet, vacuum pump and various connecting elements such as a pumping line, connection cables, and power cords. The system is controlled by a computer system that records the data using the included software. The top plate assembly consists of components used to seal the sample chamber. The probe lifting assembly can be used to hoist the probe in and out of the chamber. The Model 6000 controller is an integrated user interface that houses the electronics and the gas control valves for the PPMS. The system's vacuum pump controls the pressure in the sample chamber and regulates the gas flow rates to attain temperature control [21].

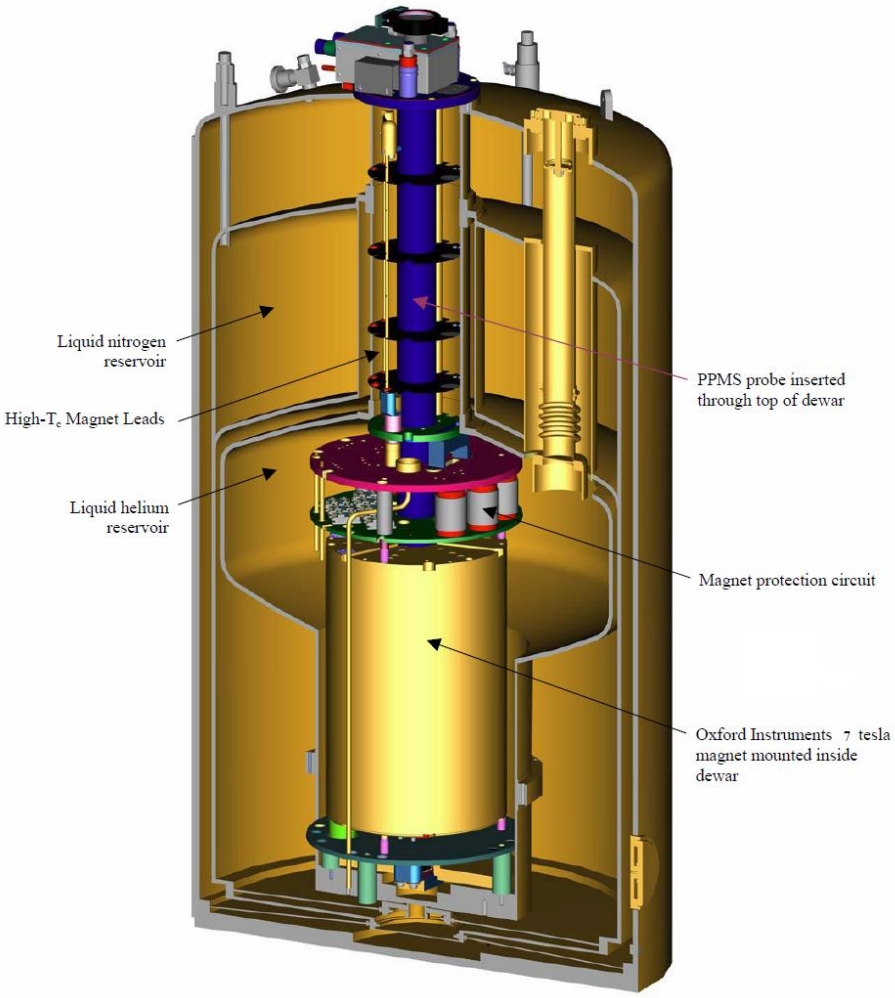

Figure 3.1: PPMS apparatus cutaway view [19]

The PPMS probe used in our magnetization measurements is shown in Figure 3.2. The probe consists of basic temperature control hardware, a superconducting magnet, a helium level meter, gas lines, sample puck connectors, and various electrical connections. The probe has two concentric tubes separated by a sealed evacuated region to prevent heat exchange. A metal bellows at the bottom of the probe protects it from being damaged by the differential thermal expansion between the outer vacuum tube and the heat shield [22].

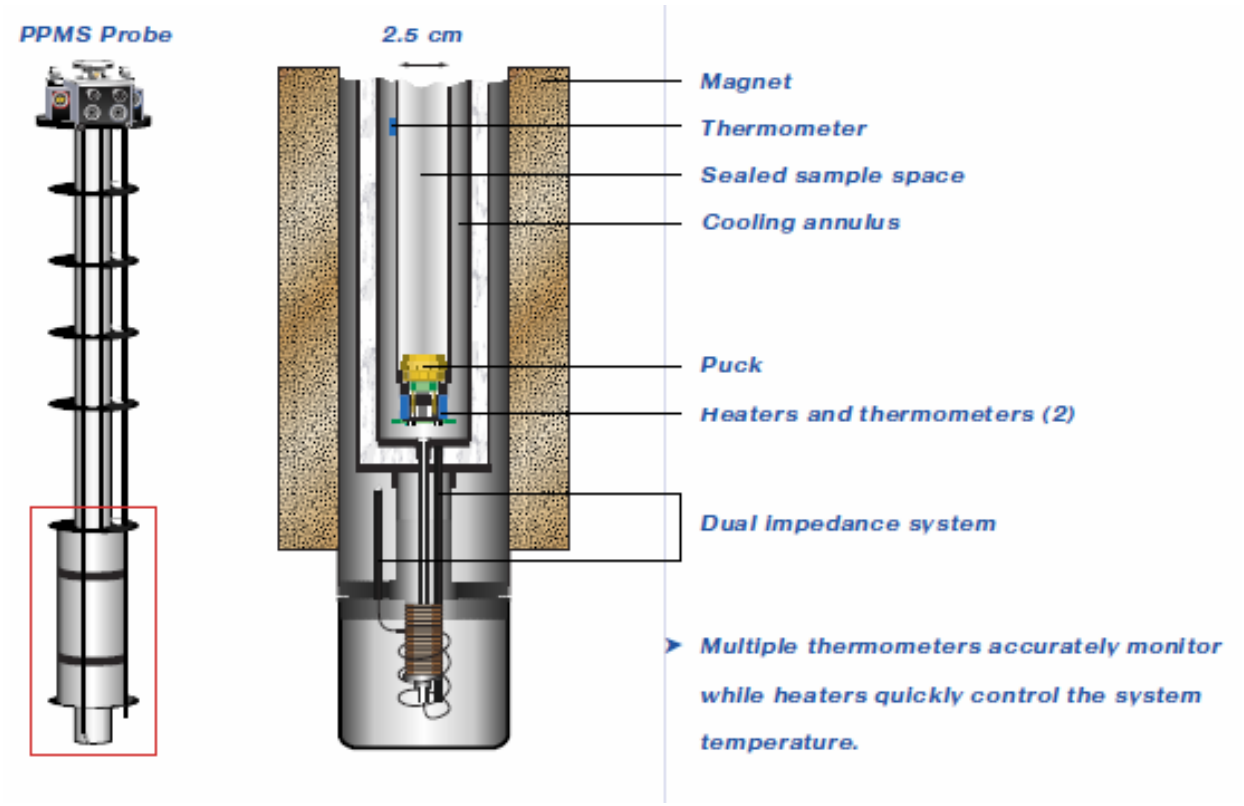

Figure 3.2: PPMS probe schematic [21]

PPMS is operated by a sequence. A sequence automates all functions the Model 6000 PPMS Controller performs, including controlling the hardware and placing the system in shutdown mode when an experiment is complete. It also automates most functions, such as setting system parameters, you can perform manually. A sequence can coordinate the operation of the PPMS hardware and of external devices and PPMS measurement options. One could use a sequence, for example, to change the temperature, current, and field and to take multiple AC resistivity measurements. The sequence file is comprised of individual sequence commands. Commands may appear in any order in the sequence. The following is the example of the sequence.

```
ACMSDF "C:\QdPpms\Data\Cristian\TU\NZFO\8\Virgin_MofH_50K.dat" 0 0 1 "" ""
REM
REM *create Log file for system variables
LOG 0 1 30.00 1073741823 1073741823 1073741823 "C:\QdPpms\Data\Cristian\TU\NZFO\8\Virgin_MofH_50K_Sys.dat" "" ""
REM
TMP TEMP 100.000000 12.000000 0
WAI WAITFOR 100 1 0 0 0 0
REM
TMP TEMP 50.000000 12.000000 0
WAI WAITFOR 100 1 0 0 0 0
REM
LPB SCANH 0.0 2000.0 100.0 21 0 0 1
WAI WAITFOR 5 0 1 0 0 0
ACMSDC 33554439 1 0 10 1 0 0 1 "" 0
ENB EOS
REM
LPB SCANH 3000.0 9000.0 100.0 7 0 0 1
WAI WAITFOR 5 0 1 0 0 0
ACMSDC 33554439 1 0 10 1 0 0 1 "" 0
ENB EOS
REM
LPB SCANH 10000.0 70000.0 100.0 13 0 0 1
WAI WAITFOR 5 0 1 0 0 0
ACMSDC 33554439 1 0 10 1 0 0 1 "" 0
ENB EOS
REM
REM
FLD FIELD 0.0 100.0 0 0
WAI WAITFOR 10 0 1 0 0 0
REM
TMP TEMP 200.000000 12.000000 0
WAI WAITFOR 200 1 0 0 0 0
REM
LOG 1 ""
REM
```

Figure 3.3: Caption of a sequence used to control PPMS

3.3 X-ray Diffraction Setup - Bruker APEX CCD Diffractometer

A Bruker-Apex CCD diffractometer was used to collect x-ray diffraction data for this experiment. The important attributes of this particular apparatus are as follows. First, this diffractometer is able to obtain accurate data even for nano-crystalline or micro-crystalline materials, which sometimes tend to be very weakly diffracting, due to its high sensitivity (1:1 imaging CCD chip) and low noise from its high gain scintillation screen and lower CCD chip cooling. Next, this apparatus excels at thermal diffuse scattering experiments because of its anti-blooming feature that restricts overflow of pixels, and high dynamic range from its optimized electronic gain. Lastly, this instrument is optimized for our particular mineralogical samples due to no spatial distortion from its large CCD chip which does not require a fiber optic taper. Other

important technical features include: a pixel resolution of 4096 x 4096, an active area of 64 mm x 64 mm, a pixel size of 15 μm x 15 μm, and a signal-to-noise ratio for a single X-ray photon of greater than 10:1 [23].

3.4 Experimental Details

Synchrotron powder XRD data from $Ni_{1-x}Zn_xFe_2O_4$ nanoparticle ensembles were collected on the X7B beamline at the National Synchrotron Light Source (Brookhaven National Laboratory) in the transmission geometry using a monochromatic x-ray beam of wavelength 0.922Å. A Mar345 flat image plate was used to detect the diffracted beam. Diffraction images, collected over an exposure time of 60 s, were eventually processed using the Fit2D software [24]. XRD data from bulk $Zn_xNi_{1-x}Fe_2O_4$ powders were collected on a Bruker APEX diffractometer using MoKα radiation (λ= 0.71073 Å). The samples were milled with paratone oil and placed on the tip of a glass fiber forming a sphere at 20 cm from the CCD-LDI-APEX1 area detector. Rotation frames were acquired using an exposure time of 60 s. The integration of the Data integration was done with the suite Bruker APEX2-2010.7-0 suite.

DC-magnetization and AC-magnetic-susceptibility measurements were carried out on our Quantum Design® Physical Property Measurement System (PPMS). Dc-magnetization curves were recorded on bulk $Zn_xNi_{1-x}Fe_2O_4$ samples upon increasing the magnetic field H from zero to 70 kOe at different temperatures between 50 and 300 K. Frequency-resolved ac-susceptibility data were collected on 10-nm average size $Zn_xNi_{1-x}Fe_2O_4$ nanoparticle ensembles upon heating from 5 to 85 K. The amplitude of the oscillating magnetic field was 5 Oe and the frequencies

used were 100, 300, 1000, 3000, and 10000 Hz. During each set measurement the powder sample was immobilized in paraffin and contained in a polycarbonate capsule.

CHAPTER 4

RESULTS AND DISCUSSION

4.1 Bulk: Dependence of the Saturation Magnetization M_s on the Zn Content x

To investigate the effect of Zn doping on the magnetic properties of bulk nickel ferrite we carried out temperature-resolved dc-magnetization, *M*, vs. magnetic field, *H*, measurements on the $Zn_xNi_{1-x}Fe_2O_4$ (x=0, 0.2, 0.4, 0.5, 0.6, 0.8, 1) series. Figure 4.1 shows M vs. H curves measured on the $NiFe_2O_4$ (x=0) sample at four different temperatures: 50 K (filled squares), 100 K (open triangles), 200 K (filled circles), and 300 K (empty squares). Figure 4.2 shows *M* vs. *H* curves measured on the $Zn_{0.5}Ni_{0.5}Fe_2O_4$ (x=0.5) sample at four different temperatures: 50 K (filled squares), 100 K (open circles), 200 K (filled triangles), and 300 K (filled circles).

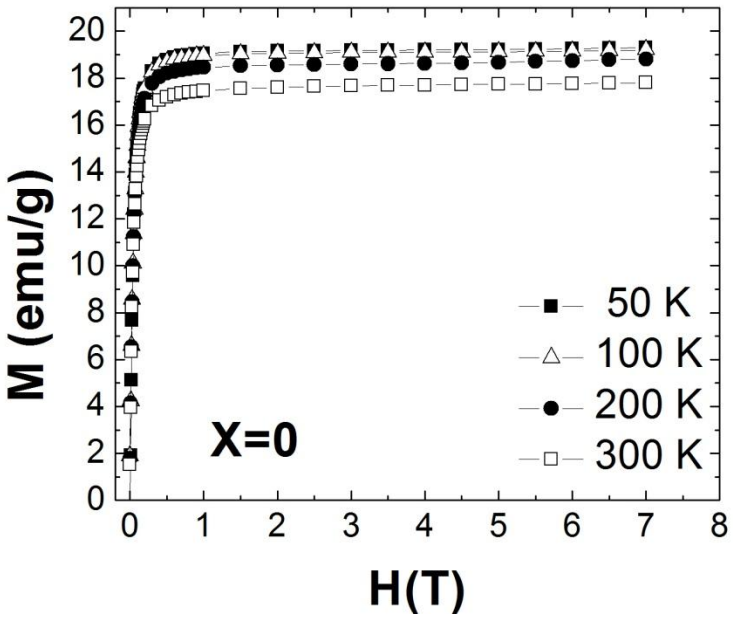

Figure 4.1: Magnetization versus temperature of $NiFe_2O_4$

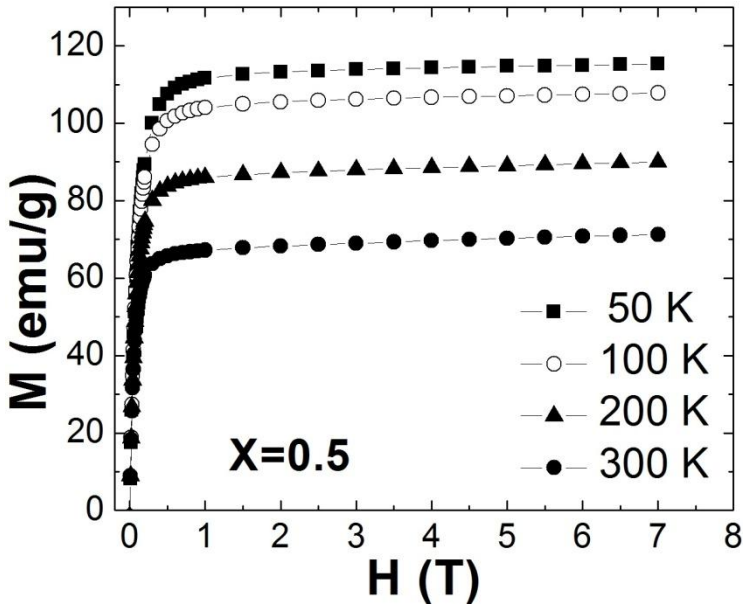

Figure 4.2: Magnetization versus temperature of $Zn_{0.5}Ni_{0.5}Fe_2O_4$

At each temperature, of every sample, the magnetization reaches a maximum value M_{max};Figure 4.3 shows the resulting M_{max} vs. T dependence (solid symbols) and a best linear fit

(solid line) whose extrapolation to T= 0 K allows the saturation magnetization M_s to be obtained for the x=0.5 sample.

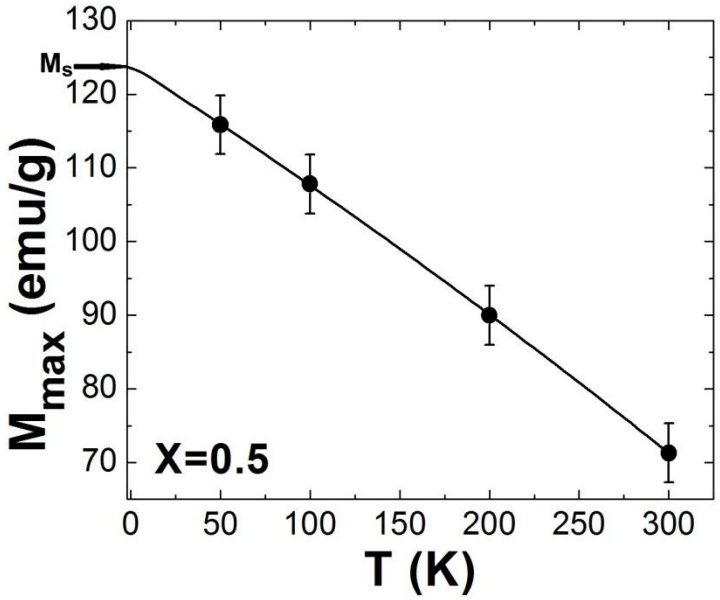

Figure 4.3: Maximum magnetization versus temperature of $Zn_{0.5}Ni_{0.5}Fe_2O_4$

Using similar data and analysis we determined the dependence of the saturation magnetization on the Zn content x. This is shown by the solid symbols in Figure 4.4, whereas the dashed line is a guide to the eyes for the M_s vs. x data. The fit clearly demonstrates that the behavior of the saturation magnetization M_s of the bulk ferrite upon Zn doping is similar to the one observed for E_B in that its nanoparticle ensemble counterpart. M_s initially (x<0.5) increases with increasing x, peaks at x=0.5, and eventually decreases upon further doping (x>0.5).

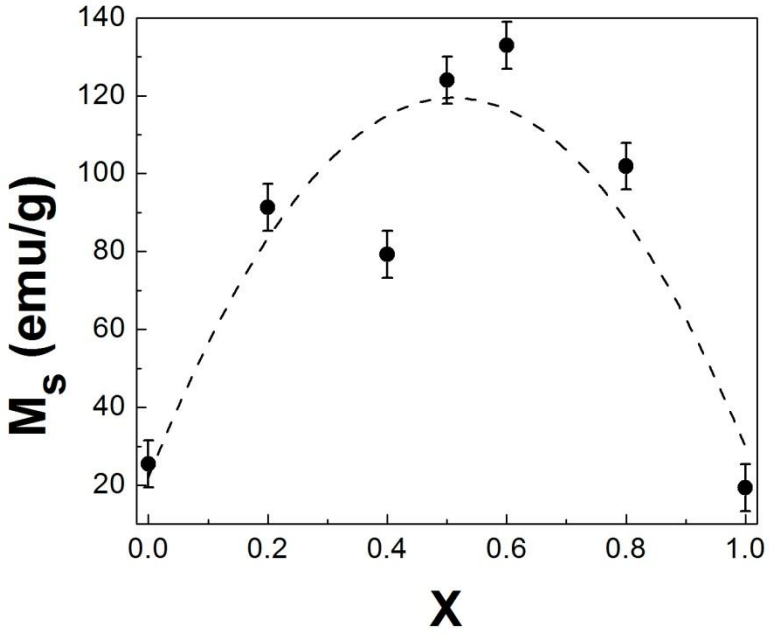

Figure 4.4: Saturation magnetization versus *x*

4.2 Nanoparticles: Dependence of the Energy Barrier to Magnetization Reversal E_B on the Zn Content *x*

Figure 4.5 shows the temperature dependence of the out of phase magnetic susceptibility χ'' measured on a 10 nm average sized $Zn_{0.5}Ni_{0.5}Fe_2O_4$ nanoparticle ensemble at five different frequencies: 100 Hz (filled circles), 300 Hz (open squares), 1000 Hz (filled triangles), 3000 Hz (open circles), and 10000 Hz (filled circles). At each frequency *f*, or, equivalently, observation time $\tau=1/2\pi f$, the χ'' vs. *T* dependence shows a well-defined peak that corresponds to the magnetic relaxation of the average sized nanoparticles in the ensemble. The peak temperature increases with the decrease of the observed relaxation time (or the increase of the measurement frequency) from *T*=36 K at $\tau = 1.59\times10^{-3}$ s (*f* = 100 Hz) to *T*=47 K at $\tau = 1.59\times10^{-5}$ s (*f* = 10000

Hz). It is well established that the temperature dependence of the relaxation time $\tau(T)$ for a system of slightly interacting magnetic nanoparticles where the relaxation occurs via the Néel mechanism (rotation of the superspin within the nanoparticle) is described by the Vogel-Fulcher equation:

$$\tau(T) = \tau_0 \exp\left[\frac{E_B}{k_B(T - T_0)}\right]. \tag{4.1}$$

Here τ_0 is a time-scale constant typically on the order of 10^{-9} -10^{-11} s, k_B is the Boltzmann constant, E_B is the energy barrier to magnetization reversal, and T_0 is a phenomenological ordering temperature which extends the basic Arrhenius-type Néel formalism by accounting for the interactions among nanoparticles. The Vogel-Fulcher law has been extensively used to probe superparamagnetism, investigate the inter-particle interaction, or determine the energy barrier E_B [25].

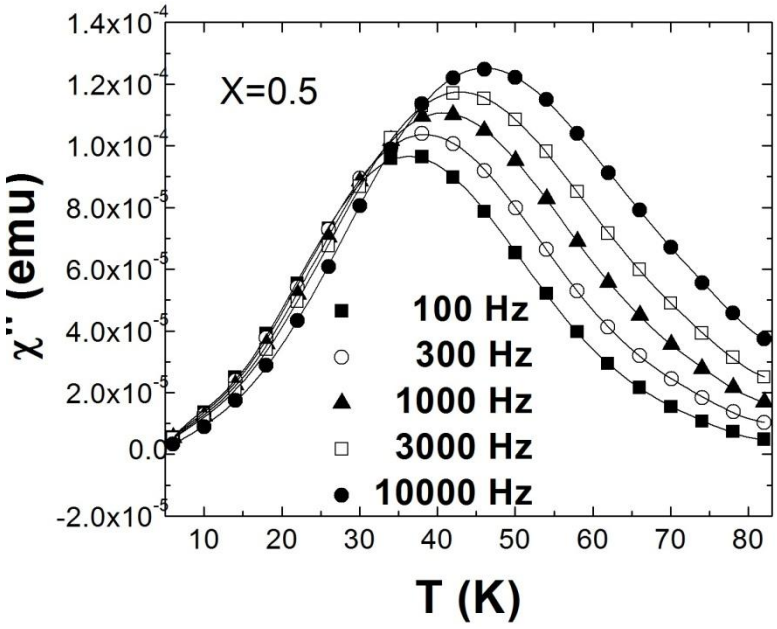

Figure 4.5: AC-magnetic-susceptibility of $Zn_{0.5}Ni_{0.5}Fe_2O_4$

As shown in Figure 4.6, the observed temperature dependence of the relaxation time $\tau(T)$ of the $Zn_{0.5}Ni_{0.5}Fe_2O_4$ (x=0.5) nanoparticle ensemble (solid symbols) is excellently described by a fit of equation (4.1) (solid line). The fit converges to low residuals R^2=0.99943, and yields parameters $\tau_0=7.77\times10^{-10}$ s, T_0 = 13K, and E_B = 0.045 eV.

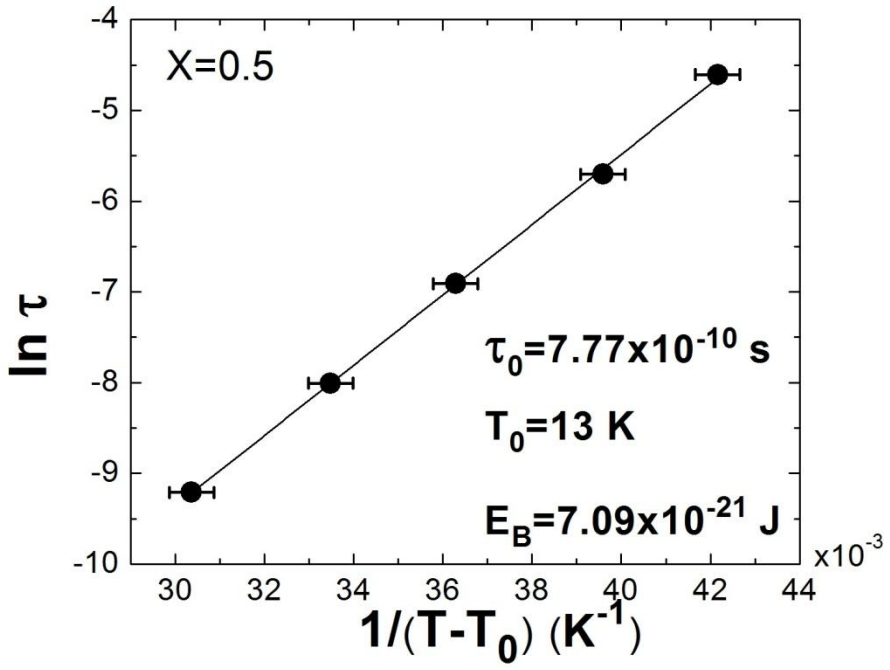

Figure 4.6: Temperature dependence of τ

Using similar data and analysis we determined the values of the energy barrier to superspin reversal E_B for four additional x values: 0.2, 0.4, 0.6, and 0.8. The solid symbols in Figure 4.7 show the resulting dependence of E_B on the Zn content x. The dashed line is used as a guide for the eye. We note that E_B initially increases with increasing x, reaches a maximum value for x=0.5, and eventually decreases upon further Zn doping (x>0.5), in excellent agreement with previous results [4].

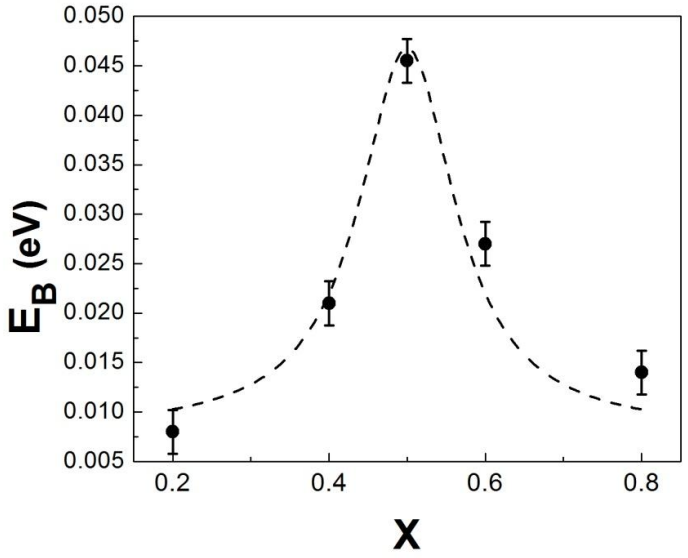

Figure 4.7: Dependence of E_B on x

4.3 LeBail Analysis of the Lattice Parameter Dependence on the Zn Content *x*

To uncover the Zn-doping induced micro-structural changes responsible for above-described magnetic behavior we first carried out a LeBail analysis of the powder XRD patterns collected from the bulk $Zn_xNi_{1-x}Fe_2O_4$ series. This was mainly aimed at investigating whether significant changes occur in the lattice of $Zn_xNi_{1-x}Fe_2O_4$ for Zn-doping values close to 0.5. Should such modification be present, their effect would be likely to carry over to the nanoparticle ensembles investigated here. This is due to the fact that although magnetic properties of nanoparticle ensembles are influenced by surface effects [26], the magnetocrystalline structure of the nanoparticles, material clearly takes precedence in terms of determining the system's magnetic behavior [27]. Figure 4.10 shows the x-ray diffraction pattern from bulk $Zn_{0.5}Ni_{0.5}Fe_2O_4$. The empty symbols represent the diffracted intensity observed at a given angle

2θ, the solid line is the corresponding best profile (LeBail) fit, the lower trace is the difference curve between the observed and the calculated intensities, and the vertical bars are the positions of the Bragg reflections. In a LeBail fit the unit cell parameters and the intensity of each individual diffraction peak are iteratively adjusted to give the best agreement with the data. This allows an accurate determination of the lattice parameter *a*; for $Zn_{0.5}Ni_{0.5}Fe_2O_4$ (*x*=0.5), we found *a*=8.41 Å. We used this (implemented in the program *FULLPROF* [28]) to find the evolution of the lattice parameter with the Zn content *x*, as well as possible changes in the unit cell symmetry. Briefly, we started with the structural information for the room-temperature phase of $NiFe_2O_4$ (space group F d -3 m and lattice parameter a=8.364 Å) to initialize the variable parameters for the LeBail fit for the undoped (*x*=0) ferrite data. The best fit parameters were then used for the next Zn-doping value, *x*=0.2, and the procedure was repeated for *x* up to *x*=1.

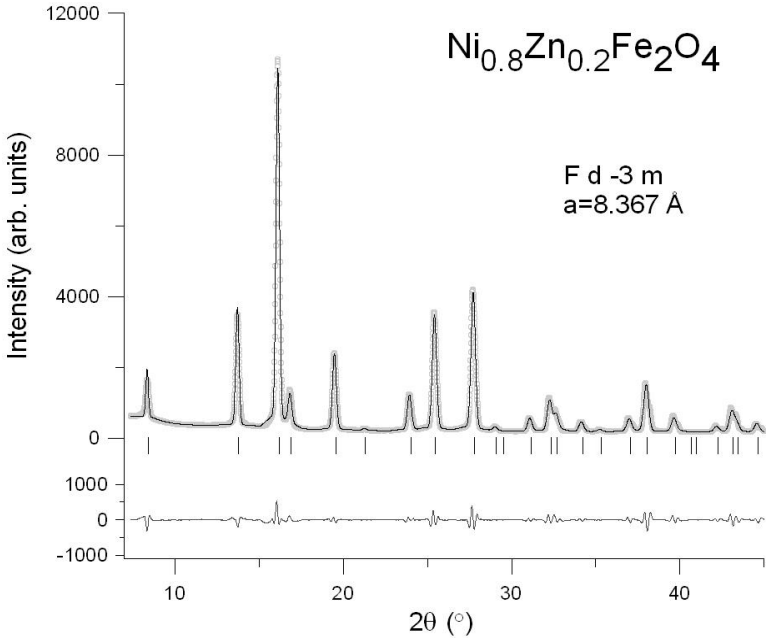

(a)

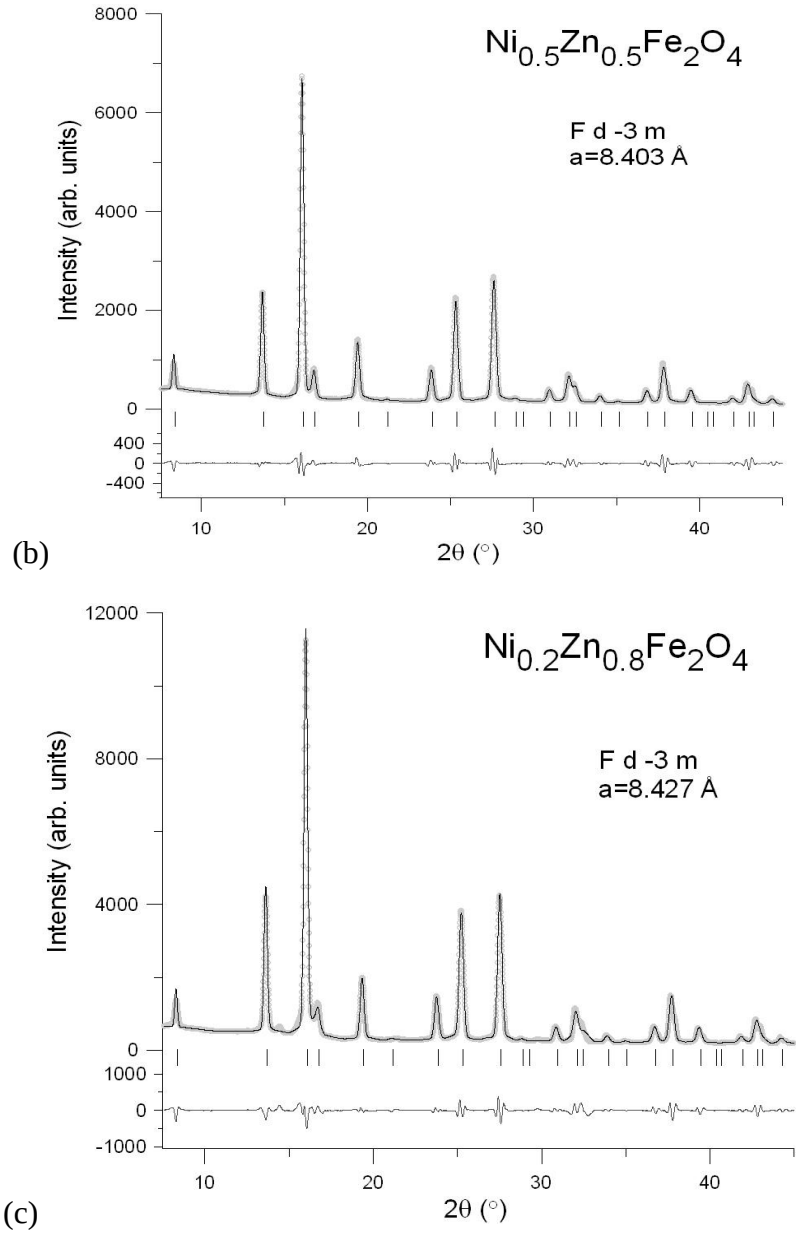

Figure 4.8: LeBail analysis

Figure 4.8a-c shows Lebail fits to x-ray diffraction data. The empty symbols in are the observed intensity (I_{obs}). The solid line is the best fit curve. The vertical bars indicate Bragg reflection positions. The solid grey line underneath is the difference between the observed and the calculated intensity (I_{obs} -I_{cal}) for (a) $Zn_{0.2}Ni_{0.8}Fe_2O_4$, (b) $Zn_{0.5}Ni_{0.5}Fe_2O_4$ and (c) $Zn_{0.8}Ni_{0.2}Fe2O4$.

The evolution of the lattice parameter upon Zn-doping obtained from the above described analysis is shown by the solid symbols in Figure 4.9. The most significant feature of this behavior is that the lattice parameter increases linearly with increasing *x* (the dashed line is a best fit of a linear function to the data), thus no significant changes, such as structural phase transitions, chemical modifications or even notable variations in the $Zn_xNi_{1-x}Fe_2O_4$ lattice parameter accompany the increase in the magnetic properties observed at *x*~0.5. This implies that the enhancement of the magnetic properties in zinc-nickel ferrite is likely determined by particular mechanism through which nickel, which resides at B (octahedral) sites of this spinel structure, is replaced by zinc.

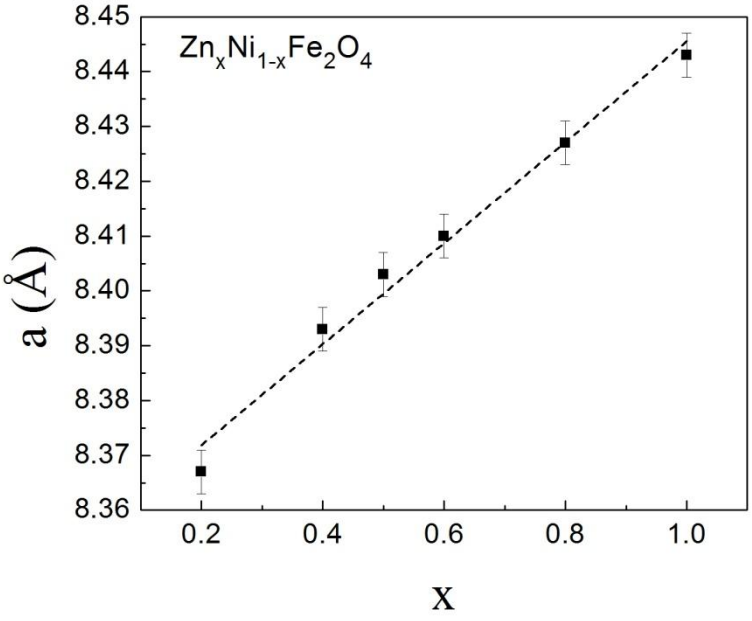

Figure 4.9: Lattice parameter variation with *x*

4.4 Rietveld Analysis of $Zn_xNi_{1-x}Fe_2O_4$

In an attempt at clarifying the crystallographic aspects of the Zn doping mechanism in $Zn_xNi_{1-x}Fe_2O_4$, we carried out Rietveld refinements to XRD data from both bulk and nanosized $Zn_xNi_{1-x}Fe_2O_4$ using the *General Structure Analysis System (GSAS)* [29]. In a Rietveld refinement one adjusts not only the parameters governing the unit cell dimensions and the peak profile shape, but also the atomic coordinates, site occupancies, and thermal parameters to obtain the best agreement with the data. We started with the known crystal structure (lattice parameter, space group, and atom coordinates) of $NiFe_2O_4$ (x=0). In this case, the A (tetrahedral) sites are completely occupied by Fe^{3+} ions, whereas half of the B (octahedral) sites are occupied by Fe^{3+} and the other half by Ni^{2+} ions. We kept all these occupancies fixed in our Rietveld refinement for the undoped nickel ferrite. We then used the resulting best-fit parameters from the x=0 refinement as input for the first Zn-doped member (x=0.2) of the $Zn_xNi_{1-x}Fe_2O_4$ series. For this and all the other doped ferrites (x=0.4, 0.5, 0.6, 0.8, 1), however, we carefully investigated the occupancies of both the A and the B sublattices. We first attempted Rietveld refinements assuming that Zn^{2+} ions directly replace Ni^{2+} in the octahedral sites, case in which we still kept the tetrahedral sites fully occupied by Fe^{3+}, while allowing the refinement of the triple occupancy (Fe^{3+}, Ni^{2+}, and Zn^{2+}) in the octahedral sublattice. We also tried structural refinements in the context of an indirect Zn-doping mechanism, by which zinc is incorporated into A (tetrahedral) sites where it displaces Fe^{3+} ions, which, in turn, migrate to the B sub-lattice and replace Ni^{2+}. Our data and analysis confirm the latter scenario for within the entire Zn-doping range ($0<x\leq1$).

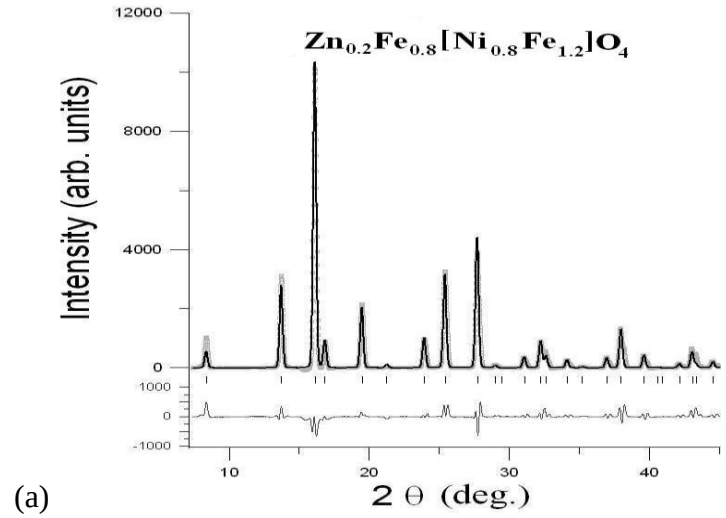

(a)

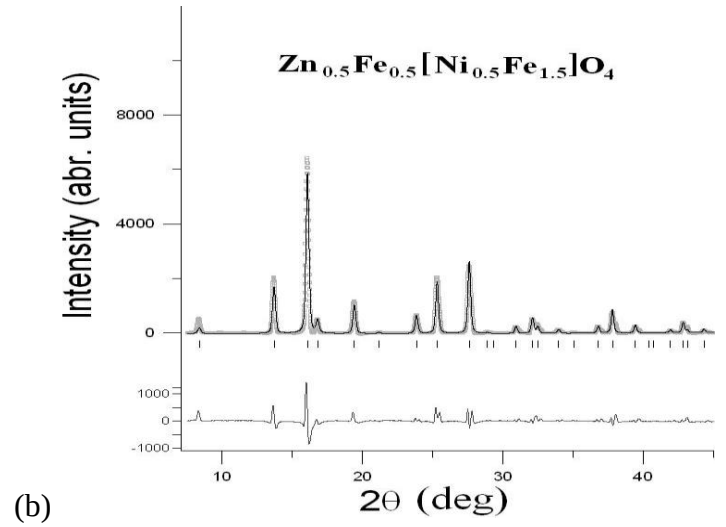

(b)

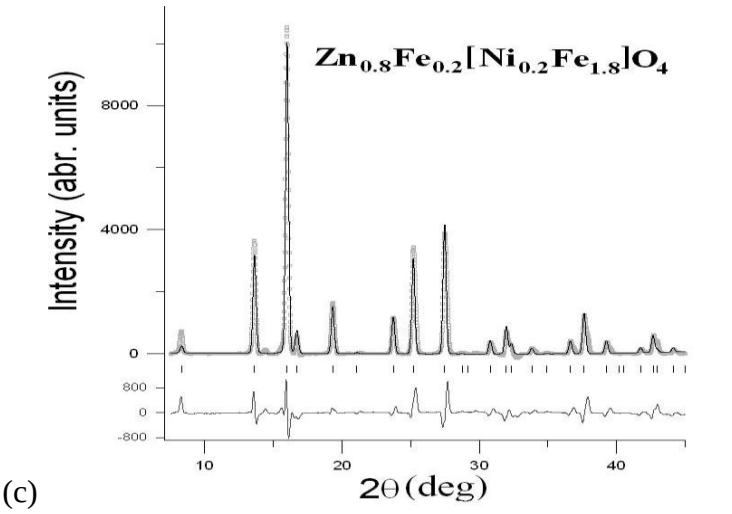

(c)

Figure 4.10: Reitveld refinements (a) $Zn_{0.2}Ni_{0.8}Fe_2O_4$, (b) $Zn_{0.5}Ni_{0.5}Fe_2O_4$ and (c) $Zn_{0.8}Ni_{0.2}Fe_2O_4$

Figure 4.10 (a) shows a Rietveld refinement to the *x*=0.5 Zn-doped nickel ferrite, where the solid line is the best fit, the empty symbols represent the scattered intensity measured as a function of the diffraction angle, the lower trace is the difference curve (between the observed and calculated patterns), and the vertical bars are reflection markers for the Bragg reflections. Allowed to vary in the refinement were the lattice parameters, histogram scale factor and zero angle, peak profile parameters, oxygen atom positions, isotropic Debye-Waller factors, as well as the occupancies of both the A and the B sites. The refinement converges upon the simultaneous variation of parameters and yields a Zn occupancy 0.47 that is remarkably close to the nominal Zn-doping value *x*=0.5. This leads to the formula $Zn_{0.47}Fe_{0.53}[Ni_{0.53}Fe_{1.47}]O_4$, where the atoms in brackets (Ni and Fe) are in the B octahedral, sites, whereas the A tetrahedral positions are partially occupied by Zn and Fe.

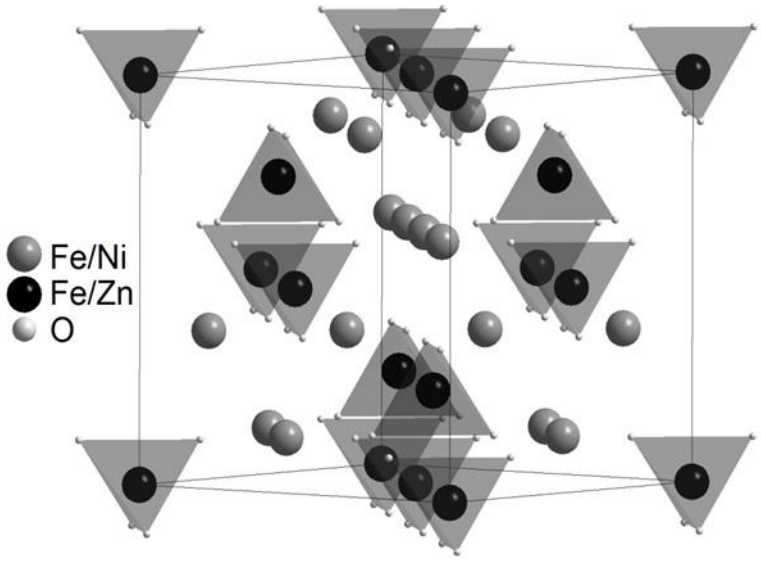

Figure 4.11: Crystal structure of $Zn_{0.5}Ni_{0.5}Fe_2O_4$

Figure 4.11 shows the three-dimensional crystal structure whereas Table 2 shows the crystallographic data and the best-fit details corresponding to this refinement.

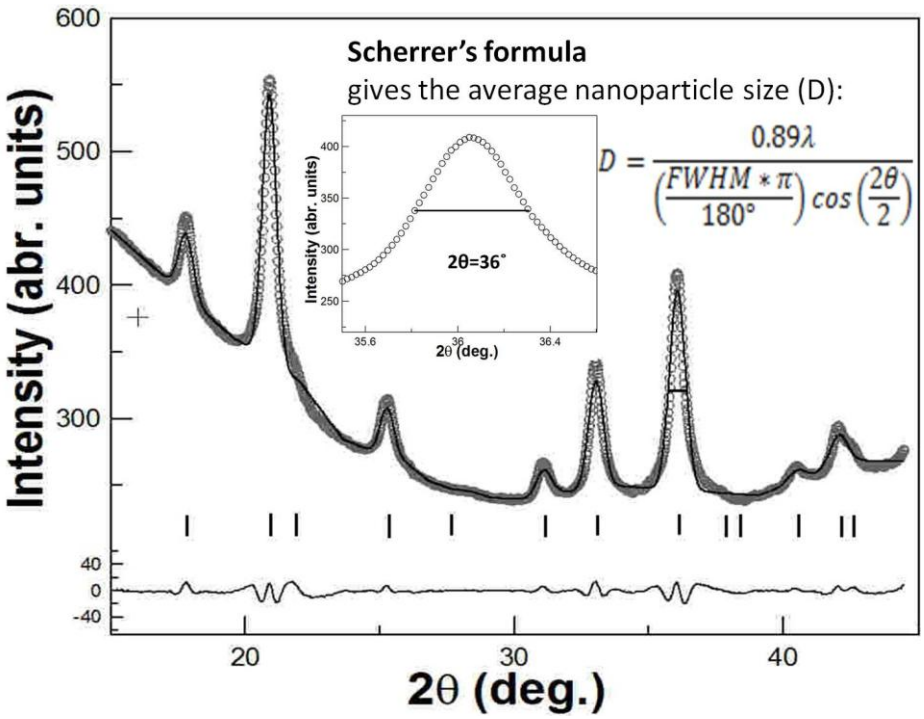

Figure 4.12 Debye-Scherrer analysis

Rietveld refinement and Debye-Scherrer confirm the ~10nm average size of the nanoparticle as shown in figure 4.12. For all Zn-doping values, we found similar results: octahedral-site nickel is indirectly replaced by zinc by its incorporation in the tetrahedral sublattice and the migration of iron ions from A to B sites. Moreover, the Rietveld refined Zn ion occupancy in the tetrahedral sites is, for all values of x, within 10% of the nominal Zn doping content, as shown in Table 3.

Table 2. Crystallographic data and details of the Rietveld refinement for $Zn_{0.5}Ni_{0.5}Fe_2O_4$

Crystallographic data	
Spacegroup	F d -3 m
a (Å)	8.41
α (deg.)	90
β (deg.)	90
γ (deg.)	90
V ($Å^3$)	594.82
ρ (g cm^3)	5.411
No. of reflections	12
No. of refined parameters	2
No. of non-hydrogen atoms	5
U_{iso}	0.02
Rietveld refinement details	
λ (Å)	0.7107
(sin θ/λ ($Å^{-1}$))	0.92
Step length (deg.)	0.01
R_p	0.1281
R_{wp}	0.1856
χ^2	11.76

Table 3 Comparison between nominal Zn doping in $Zn_xNi_{1-x}Fe_2O_4$ and the Zn content in the A (tetrahedral) sublattice obtained from Rietveld refinements.

$Zn_xNi_{1-x}Fe_2O_4$	
Nominal Zn doping (x)	Zn content in A (tetrahedral) site from Reitveld refinement
0.2	0.26
0.4	0.44
0.5	0.47
0.6	0.58
0.8	0.78
1	0.96

Our results represent strong and direct evidence for the validity of the above-described indirect replacement mechanism of Ni^{2+} by Zn^{2+} in the complex ferrite. This is highly significant, because the gradual incorporation of Zn in the A sublattice offers an explanation for the very distinct magnetic property behavior observed both in bulk and in nanosized $Zn_xNi_{1-x}Fe_2O_4$ ferrites upon Zn doping. Indeed, as first noted in reference 3 [3], replacing magnetic Ni by nonmagnetic Zn doped in the A sites initially enhances the magnetic properties of the title material. This is based on the magnetic structure of the inverse spinnel ferrite, where the overall magnetic moment results from the difference between the magnetic moments of the B and A sublattices. Consequently, reducing the magnetic moment in the A sites (by replacing magnetic Fe^{3+} with nonmagnetic Zn^{2+}) actually enhances the magnetization of the ferrite. Obviously, this effect becomes more pronounced as the Zn content, *x* increases. At the same time, however, increasing *x* gradually leads to non-colineal arrangements of the atomic spins in the B lattice, a competing effect that tends to reduce the magnetization of the complex ferrite upon Zn doping. As it is reasonable to believe that the latter

effect is more pronounced at larger x values, the observed magnetic behavior is entirely consistent with a crossover between the two above-described competing magnetocrystalline effects at x~0.5.

CHAPTER 5

CONCLUSION

We have investigated the microscopic structures that lead to the enhancement of magnetic properties in bulk and nanoparticle ensembles of zinc-doped nickel ferrite $Zn_xNi_{1-x}Fe_2O_4$. We found that that both the nanoparticle energy barrier to magnetization reversal E_B, and the bulk saturation magnetization, M_s increase with increasing x, reach a maximum at x~0.5, and eventually decrease upon further doping. Yet, our data show no significant structural modifications at x~0.5; the lattice parameter of $Zn_xNi_{1-x}Fe_2O_4$ increases linearly with x, and the same inverse spinel crystal structure persist throughout the entire zinc doping range. Instead we found evidence of an indirect doping mechanism, where zinc is incorporated into A (tetrahedral) sites where it displaces Fe^{3+} ions, which, in turn, migrate to the B (octahedral) sub-lattice and replace Ni^{2+}. This scenario leads to competing effects consistent with the observed magnetic property enhancement at x~0.5.

REFERENCES

[1] S. Morup et al., Phys. Rev. Lett., 70, 134416()2004

[2] C. Martin et al., Phys. Rev. B., 63 174402(2001)

[3] R. Arulmurugan et al., J. Magn. Magn. Mater., 288, 470-477(2005)

[4] J.T. Galindo et al., Appl. Phys. A., 87, 743-747(2007)

[5] A. LeBail, J. Appl. Cryst.,37, 911-924(2004)

[6] H. M. Rietveld, J. Appl. Cryst., 2, 65-71(1969)

[7] D. J. Griffiths, Introduction to Electrodynamics (1999)

[8] J. D. Jackson, Classical Electrodynamics (1998)

[9] G. Pollack and D. Stump, Electromagnetism (2001)

[10] S. R. Shinde et al., Phys. Rev. Lett., 92, 16(2004)

[11] H.Vogel, Phys. Z., 22, 645(1921)

[12] G. S. Fulcher and J. Amer, Ceram. Soc., 8, 339(1925).

[13] C. Kittel, Introduction to Solid state physics (2005)

[14] E.Lifshin, X ray characterization of materials (1999)

[15] C. Suryanarayana and M. G. Norton, X-ray diffraction: A practical approach (1998)

[16] C. N. Chinnasamy et al., Phys. Rev. B., 63, 184108(2001)

[17] R. S. Tebble and D. J. Craik, Magnetic materials (1969)

[18] H. Perron et al., J. Phys.: Condens. Matter., 19, 10(2004)

[19] Quantum Design Physical Property Measurement System, Retrieved from http://www.qdusa.com/sitedocs/productBrochures/16TPPMS7.pdf

[20] Quantum Design Physical Property Measurement System, Retrieved from http://www.qdusa.com/sitedocs/productBrochures/ppms_9_06.pdf

[21] Quantum Design Physical Property Measurement System, Retrieved from http://qdusa.com/products/ppms.html

[22] M. H. Chen, Magnetic phase transitions in praseodymium-barium doped manganites (2007)

[23] Bruker APEX X-Ray diffractometer, Retrieved from http://www.bruker-axs.com/smart_apex_ii.html

[24] A. P. Hammersley, FIT2D V 10.3 Reference manual V 4.0 (1998)

[25] E. Romanus et al., J. Nanotechnol., 14, 1251-1254(2003)

[26] M. P. Proenca et al., Phys. Chem. Chem. Phys., 19, 9561-9567(2011)

[27] V. Trukhanov et al., J. Phys.: Condens. Matter., 15, 1783(2003)

[28] J. Rodriguez-Carvajal, An Introduction to the Program Fullprof 2000 (2001)

[29] A. C. Larson and R. B. Von Dreele, General Structre Anaylis System (2004)

CURRICULUM VITA

Kanokporn Chattrakun was born on August 19, 1985 in Phichit, Thailand. The first daughter of Prapas Chattrakun and Sombat Chattrakun, she earned her B.Sc. in Physics from Mahidol University in 2008. In 2009, she joined the department of Physics at the University of Texas at El Paso as a graduate student with a C. Sharp Cook Graduate Scholarship from the department. She was awarded her M.S. in Physics degree in May 2011 and will begin her doctoral studies with the department of Physics at the University of Arizona in August 2011.